ADVANCED ELECTRONIC MATERIALS
www.advelectronicmat.de

Strong Piezoelectricity in 3R-MoS_2 Flakes

Hamida Hallil, Weifan Cai, Kang Zhang, Peng Yu, Sheng Liu, Ran Xu, Chao Zhu, Qihua Xiong, Zheng Liu, and Qing Zhang**

Distinct from conventional 2H-MoS_2, recently synthesized 3R-MoS_2 exhibits a noncentrosymmetric atomic structure of the trigonal "building blocks" and, thus, remarkable piezoelectric characteristics of ultrathin 3R-MoS_2 flakes are predicated theoretically. This paper reveals, for the first time, very high piezoelectricity in 3R-MoS_2 flakes experimentally. Through applying mechanical stress to a 48 nm 3R-MoS_2 flake, a high output power density of 65 mW m^{-2} is obtained and is at least one order larger than those from the corresponding monolayer MoS_2 flake. With out-of-plane lateral piezoresponse force microscopy technique, the two piezoelectric coefficients d_{33} and d_{13} are analyzed to be ≈0.9 and ≈1.6 pm V^{-1}, respectively. These piezoelectric coefficients are not apparently dependent on the flake thickness. The findings suggest that 3R-MoS_2 is of excellent piezoelectric properties and it can be an excellent material for novel piezoelectric devices.

1. Introduction

Advanced technologies promote mass production of thin piezoelectric microelectromechanical systems with different functions, such as radiofrequency filters based on different acoustic waves propagation modes,[1,2] light modulators via the acousto-optic effect,[3–5] pressure and strain sensors,[6] bio and chemical sensors,[7–9] etc. However, when the thickness of conventional piezoelectric materials, such as quartz, lithium niobate, PZT substrates, or other piezoelectric thin film, is reduced to about 1 µm, the negative impacts of their defective surfaces and their crystallographic texture on the piezoelectric properties become significant so that acoustic waves are strongly scattered and or absorbed.[10] This disadvantage restricts the materials from being employed in high frequency (>10 GHz) acoustic devices. In addition, conventional piezoelectric materials are in general very brittle and thermally insulating. The devices based on these materials are of low mechanical flexibility and poor thermal stability. To meet a wide spectrum of applications, novel piezoelectric materials and devices with unique functionalities and high performances are in high demands.

In the last decade, in-depth understanding of 2D nanomaterials has significantly boosted the ultrathin materials for nanoelectronic applications. Recent studies suggest that the mechanical properties of 2D transition metal dichalcogenides materials, including MoS_2, are comparable to graphene. The elastic modulus of CVD and exfoliated monolayer MoS_2 reported so far is 171 ± 11 N m^{-1}, nearly half the value of graphene that is known as the strongest material.[11] Few layer MoS_2 nanosheets are of a very high Young's modulus E = 0.33 ± 0.07 TPa, only one third lower than that of exfoliated graphene.[12] In addition, recent first-principle studies suggest that the piezoelectric coefficients of monolayer or few layer MoS_2, $MoSe_2$, WS_2, and WSe_2 flakes could be sufficiently large or comparable to those of conventional bulk piezoelectric materials, such as α-quartz, wurtzite GaN, and wurtzite AlN.[13,14] Indeed, the measured lateral piezoelectric coefficient of monolayer MoS_2 along its armchair direction is 1.5 times greater than that of quartz.[15] In addition, the thermal conductivity

H. Hallil, Z. Liu, Q. Zhang
UMI 3288 CINTRA CNRS-NTU-THALES
Nanyang Technological University
Research Techno Plaza
50 Nanyang Drive, Singapore 637553, Singapore

H. Hallil, W. Cai, K. Zhang, R. Xu, Z. Liu, Q. Zhang
Centre of Micro-/Nanoelectronics (CMNE)
School of Electrical and Electronic Engineering
Nanyang Technological University
Singapore 639798, Singapore
E-mail: eqzhang@ntu.edu.sg

H. Hallil
University of Bordeaux
Bordeaux INP
CNRS
IMS UMR 5218, Talence F-33405, France
E-mail: hamida.hallil-abbas@u-bordeaux.fr

The ORCID identification number(s) for the author(s) of this article can be found under https://doi.org/10.1002/aelm.202101131.

DOI: 10.1002/aelm.202101131

P. Yu
School of Materials Science and Engineering
Sun Yat-sen University
Guangzhou, Guangdong 510275, China

S. Liu, Q. Xiong
Division of Physics and Applied Physics
School of Physical and Mathematical Sciences
Nanyang Technological University
Singapore 637371, Singapore

C. Zhu, Z. Liu
School of Materials Science & Engineering
Nanyang Technological University
Singapore 639798, Singapore

Q. Xiong
State Key Laboratory of Low-Dimensional Quantum Physics
and Department of Physics
Tsinghua University
Haidian District
Beijing 100084, P. R. China

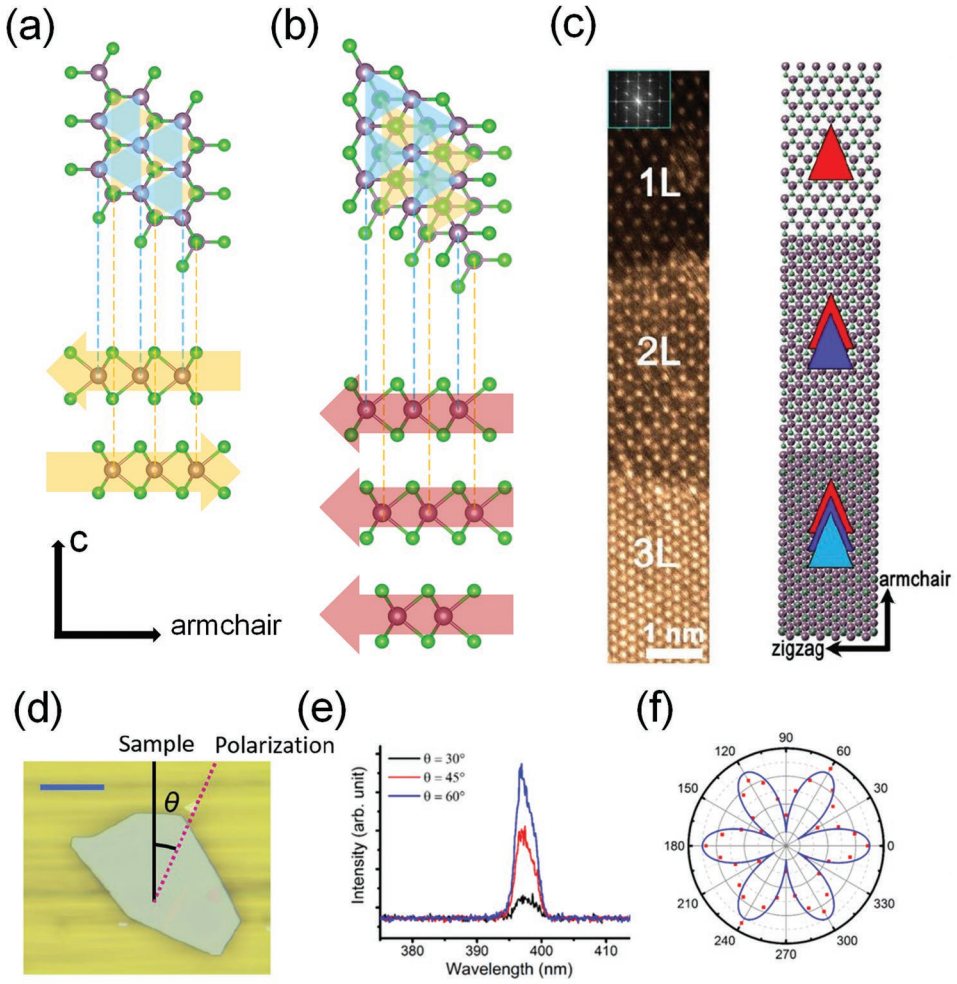

Figure 1. Top and side views of the atomic structures of a) 2H and b) 3R bilayer MoS_2; c) an atomic resolution STEM-ADF image of monolayer MoS_2, bilayer and trilayer 3R-MoS_2 and corresponding FFT pattern shown in the inset; d) the optical image of the 3R-MoS_2 flake; e) the SHG signal at three θ angles and f) the angle dependence of the SHG intensity of the 3R-MoS_2 flake shown in (d).

of MoS_2 flakes is found to be 40–70 W m^{-1} k^{-1},[16–19] about an order of magnitude larger than that of crystalline quartz (4–6 W m^{-1} k^{-1}), lithium niobate (3–5 W m^{-1} k^{-1}) and lithium tantalate (8 W m^{-1} k^{-1}).[20] This means this 2D material could dissipate heat efficiently and enhance the thermal stability and durability of piezoelectric devices. Taking all these into consideration, the employment of the atomic-layer piezoelectric materials could enable to miniaturize piezoelectric devices, a key to raise the operating frequencies.

Till now, the state-of-the-art research is still focused on the piezoelectric characteristics of monolayer MoS_2 and 2H-MoS_2 flakes or theoretical studies of 3R-MoS_2 flakes. The measured piezoelectric coefficient e_{11} for monolayer MoS_2 is 2.9×10^{-10} C m^{-1}.[13] The theoretical calculations showed that d_{33} and d_{31} of 3R MoS_2 are 0.27 and –0.21 pm V^{-1}.[13] However, direct observation of the piezoelectricity of 3R-MoS_2 flakes has not been reported yet. In this context, we present the first experimental evidence of strong piezoelectricity of exfoliated 3R-MoS_2 flakes. These findings reveal the promising piezoelectric properties of 3R-MoS_2 flakes and pave the way to design and engineer new nanogenerators and ultrahigh frequency piezoelectric devices for various applications.

2. Results and Discussion

2.1. Structure Analysis of 3R-MoS_2 Flakes

Conventional 2H-MoS_2 material (**Figure 1**a) shows the centrosymmetry of the hexagonal structure with the space group of 6*mm*.[13,21] One major obstacle of making use of 2H-MoS_2 flakes for piezoelectric applications is that its piezoelectric response only occurs in few odd atomic layers.[22–25] All even atomic layers of 2H-MoS_2 flake show negligible piezoelectric response due to the centrosymmetry that cancels piezoelectric polarization between alternating layers.[23] Such a characteristic greatly hampers the efforts to explore 2H-MoS_2 material for piezoelectric applications.[26,27]

In contrast, 3R-MoS_2 material has been theoretically predicted to be of promising piezoelectric properties. First of all, the atomic structure of 3R-MoS_2 (Figure 1b) does not have a centrosymmetry of the trigonal "building blocks" and, thus, 3R-MoS_2 belongs to the space group of *R*3*m*. The noncentrosymmetric of 3R-MoS_2 flakes can induce strong piezoelectricity, regardless of the number of stacking layers It has been

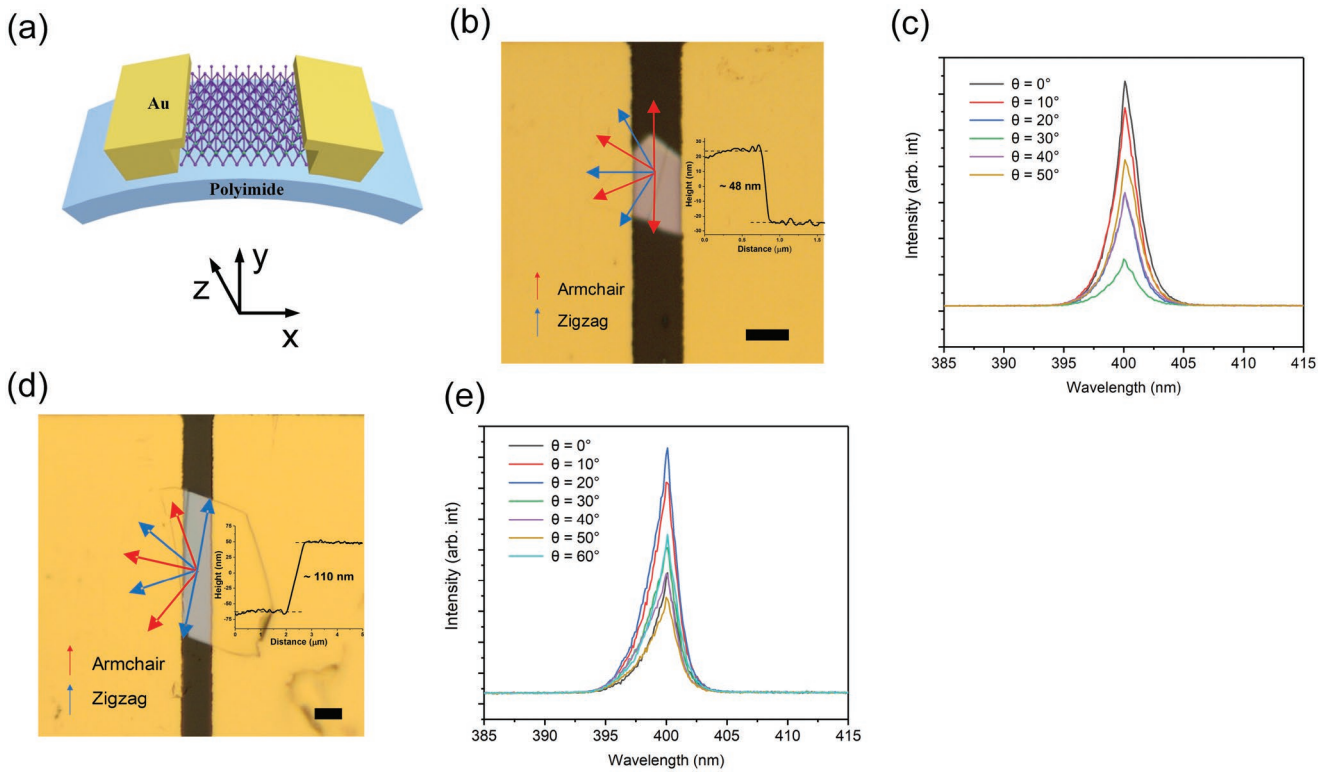

Figure 2. The 3R-MoS_2 devices with two electrodes and the orientation of the flakes. a) Illustration of a mechanical strain applied to the 3R-MoS_2 flakes with respect to the edges of the two electrodes. b) Optical image of an aligned 3R-MoS_2 flake device and the high profile of the flake, scale bar is 5 μm. c) The SHG for the aligned device in (b), suggesting that the armchair orientation is along $\theta = 0°$, 60°, and 120°, etc, and the zigzag orientation is along $\theta = 30°$, 90°, and 150°, etc.; d) Optical image of a nonaligned 3R-MoS_2 flake device and the high profile of the flake, scale bar is 5 μm. e) The SHG for the nonaligned device in (d), indicating that the armchair is along $\theta = 20°$, 80°, and 140°, etc, and the zigzag is along $\theta = 50°$, 110°, and 170°, etc.

theoretically predicated that large in-plane piezoelectricity exists in 3R MoS_2 from monolayer to bulk (the highest in-plane piezoelectric coefficient e_{22} = 0.64 C m^{-2} is predicted for the five layers).[28] In addition, the atomic layered material is much more flexible than any other conventional piezoelectric materials known.[29–33] 3R-MoS_2 based piezoelectric devices could thus be easily integrated with other flexible electronic devices.

In this study, 3R-MoS_2 flakes were prepared by mechanical exfoliation of a CVD 3R-MoS_2 crystal onto polyimide or Au/SiO_2/Si and SiO_2/Si substrates (see Experimental section). As illustrated in Figure 1b, 3R-MoS_2 flake preserves a noncentrosymmetric structure in bulk with a unit cell of S-Mo-S. Figure 1c shows the atomic lattice structures of monolayer, bilayer, and trilayer 3R-MoS_2 using scanning transmission electron microscopy (STEM) annular dark-field (ADF) images. The simulated structure (to the right of the STEM image) agrees well with the structure illustration of 3R-MoS_2 flake in Figure 1b. The inset in Figure 1c shows the selected area electron diffraction (SAED) patterns. The hexagonal symmetry of the atomic arrangement manifests that 3R MoS_2 flake consist of a single crystal domain.

Second-harmonic generation (SHG) microscopy was employed to study the crystalline symmetry of the MoS_2 flakes. It has been well-accepted that 2H-MoS_2 flakes have no SHG due to their central symmetry. In contrast, 3R-MoS_2 flakes break the inversion symmetry, and they should in principle have SHG.[34,35] As shown in Figure 1d,e, 3R-MoS_2 flakes with thickness ≈30 nm show a significant SHG, being consistent with the previous report. In addition, since the polarization-resolved SHG is crystalline orientation dependent, the SHG intensity versus the sample rotation angle could unveil the orientation of each 3R-MoS_2 flake.[35] A sixfold angle dependent of SHG intensity is illustrated in Figure 1f, which is caused by exciting the 3R-MoS_2 flake with linear polarized light under normal incidence and then filtering the SHG response with a linear polarizer. The parallel intensity SHG response pattern follows the relationship of $I_{\parallel}(2\omega)$ which is proportionel to $\cos^2(3\phi + \theta)$, where ϕ represents the angle between the mirror plane in the crystal structure and the polarization of the pump beam, and θ is the rotation of the armchair directions of the crystal relative to the y axis.[21,35–37] The maximum SHG response coincide with the armchair directions of the 3R-MoS_2 flakes. The blue fitting curve shown in Figure 1f agrees with the experimental data with $\theta = 0°$, representing that the armchair initially was along with the input laser polarization.

2.2. Piezoelectricity of 3R-MoS_2 Flakes

The piezoelectric properties were investigated by applying mechanical uniaxial strains on the 3R-MoS_2 flakes which were placed on polyimide substrates. The 3R-MoS_2 flakes could be stretched through bending the polyimide substrates, as shown in **Figure 2**a. The x and y axis corresponds to the directions

perpendicular and parallel to the edges of the electrodes, respectively. The z axis represents the direction out-of-plane of the 3R-MoS_2 flakes.

The applied uniaxial strain to the 3R-MoS_2 flakes was estimated by calculating the bending radius through the travel distance of a linear motor.[24,25,38] The calculation of the applied uniaxial strain can be found in Figure S1 and Table S1 (Supporting Information).

A 48 nm 3R-MoS_2 flake whose zigzag axis and armchair axis were placed perpendicular and parallel to the edge of the electrode is named as an aligned device and its armchair orientation (at 0°) was confirmed by using SHG characterization (see Figure 2b, c). Another 110 nm 3R-MoS_2 flake device presented in Figure 2d is named nonaligned device as the 3R-MoS_2 flake orientated neither perpendicular to the armchair nor zigzag axis as also confirmed by HSG in Figure 2e.

It is known that piezoelectric charges occur at the two terminals of a piezoelectric material when it is subject to a mechanical strain. The polarity of the induced charges is determined by the strain direction with respect to the crystalline orientation. The occurrence of these piezo-charges attracts opposite sign charges to the electrodes that are in contact with the terminals, inducing a transient current in the closed external circuit or a transient voltage between the two unconnected terminals. Once the strain is released, the piezo-charges are neutralized. As a result, the attracted charges in the electrodes must be released back to the circuit, producing an opposite flowing transient current or voltage. Indeed, this phenomenon was well reported in strained monolayer MoS_2.[15]

To exclude any possible electrical influences from the substrate, a bare polyimide substrate and a 2H-MoS_2 flake on the polyimide substrate were characterized under a tensile strain of 0.47%, respectively. No measurable induced short-circuit transient currents (or open-circuit voltages) were detected, as shown in Figure S2 (Supporting Information).

In comparison, apparent transient output voltage and current were observed once 3R-MoS_2 flakes were subject to a strain. When the 48 nm aligned 3R-MoS_2 flake was stretched along the x direction (**Figure 3**a), a positive open-circuit voltage pulse of 102 mV and a positive short-circuit current pulse of 210 pA were observed (Figure 3b,c). Once the strain was released, a negative voltage pulse and a negative current pulse were detected. More importantly, when an aligned 3R-MoS_2 flake was stretched along x direction, the polarities of the generated short-circuit current and open-circuit voltage were clearly opposite to those caused by stretching along its y direction. The dependence of the piezoelectric outputs on the directions of the principal strain in 3R-MoS_2 was deduced in Supporting Information. The in-plane polarization along the y axis (see Figure S3, Supporting Information) can be expressed as $P_2 = e_{22}$ (ε_2-ε_1), whereas e_{22} is the piezoelectric stress coefficient along y, ε_1 and ε_2 are strains along the x, y axis. The polarization P_2 output signs could be reversed when strain is rotated 90°, which is consistent with the experimental results. For the nonaligned 110 nm 3R-MoS_2 flake, when the tensional strain along the x axis was applied (Figure 3d) a positive voltage pulse of 40 mV and a positive current pulse of 110 pA were observed (Figure 3e, f). On the contrary, the polarities of the generated current and voltage in response to the strain in the x-direction for the nonaligned flake were consistent with that of strain in the y-direction (see Figure S4, Supporting Information). This finding might be attributed to the unique coupling function of the in-plane and out-of-plane piezoelectricity in these 3R-MoS_2 flakes. Similar observation was reported for piezoelectric α-In_2Se_3 flakes, where the in-plane and out-of-plane piezoelectricity were utilized to explain the findings.[39,40] Thus, these findings suggest that the piezoelectric response of the 3R-MoS_2 flake was more significant than that from a monolayer MoS_2 flake.[15] The piezoelectric signals were also found highly stable and repeatable. A mechanical durability test was performed on the aligned 3R-MoS_2 flake with a bending cycle frequency of 0.4 Hz for 30 min, as shown in Figure 3g. After 720 cycles, the induced peak current only decreased from ≈210 to ≈180 pA, about 86% of the initial value (Figure 3h).

To better evaluate the mechanical to electric power conversion performance, the peak piezoelectric output voltage and current as a function of external loading resistance from the aligned sample were measured at a tensile strain of 0.47% and the strain frequency of 0.4 Hz in Figure 3i. The maximum instantaneous power was around 11.8 pW at a load resistance of 200 MΩ, as displayed in Figure 3j. As the area of the aligned 3R-MoS_2 flake was estimated around 182 μm^2, the maximum converted electric power density was around 65 mW m^{-2}. To our best knowledge, this power density was at least one order of magnitude larger than any other monolayer MoS_2 flakes reported so far, in which the applied 0.47% tension strain for our study was the smallest, as listed in Table S2 (Supporting Information).

Alternatively, when an electric field is applied to a piezoelectric material, mechanical stresses/strains must be induced (reverse piezoelectric effect). Here, we could determine the lateral and out of plane piezoelectric coefficients (d_{33} and d_{13}) with piezoresponse force microscopy (PFM).[15,41–43] In fact, for thin piezoelectric film applications, d_{33} and d_{13} are the most important piezoelectric parameters.[44,45] For our 3R-MoS_2 flakes, d_{33} is the induced strain in direction 3 (the z axis direction) while the flakes are electrically polarized in direction 3 (z) (**Figure 4**a). The d_{13} stands for the induced strain in direction 3 (z) (perpendicular to the flakes) with electric field applied in direction 1 (x), as shown in **Figure 5**a.

For the characterization of d_{33}, we transferred and measured 20 pieces of 3R-MoS_2 flakes through PFM on an Au/Ti/SiO_2/Si substrate. The flakes were of the thickness between 4 and 90 nm. A Pt/Ir coated conductive tip with a force constant of 2.8 N m^{-1} was used to apply an electric field (AC signal) in a dual AC resonance tracking PFM mode through the 3R-MoS_2 flakes. By applying a signal with a drive amplitude V_{ac} sweeping from 0 to 1.5 V at step of 0.25 V on the tip, the deflection of the conductive tip caused by the expansion and contraction of the flake could reveal the different amplitude and phase of the piezo generated strains in the vertical direction.

Several areas were selected from the PFM amplitude image to quantitatively evaluate d_{33}. The inverse optical lever sensitivity (InvOLS), a necessary parameter for the cantilever spring constant calculation, was calibrated. The z direction displacement of the tip could be derived by multiplying the InvOLS with the deflection signals. Due to the AFM sharp tip, the electric field between the tip and conductive substrate is not uniform. As a result, the relation between the piezoelectric

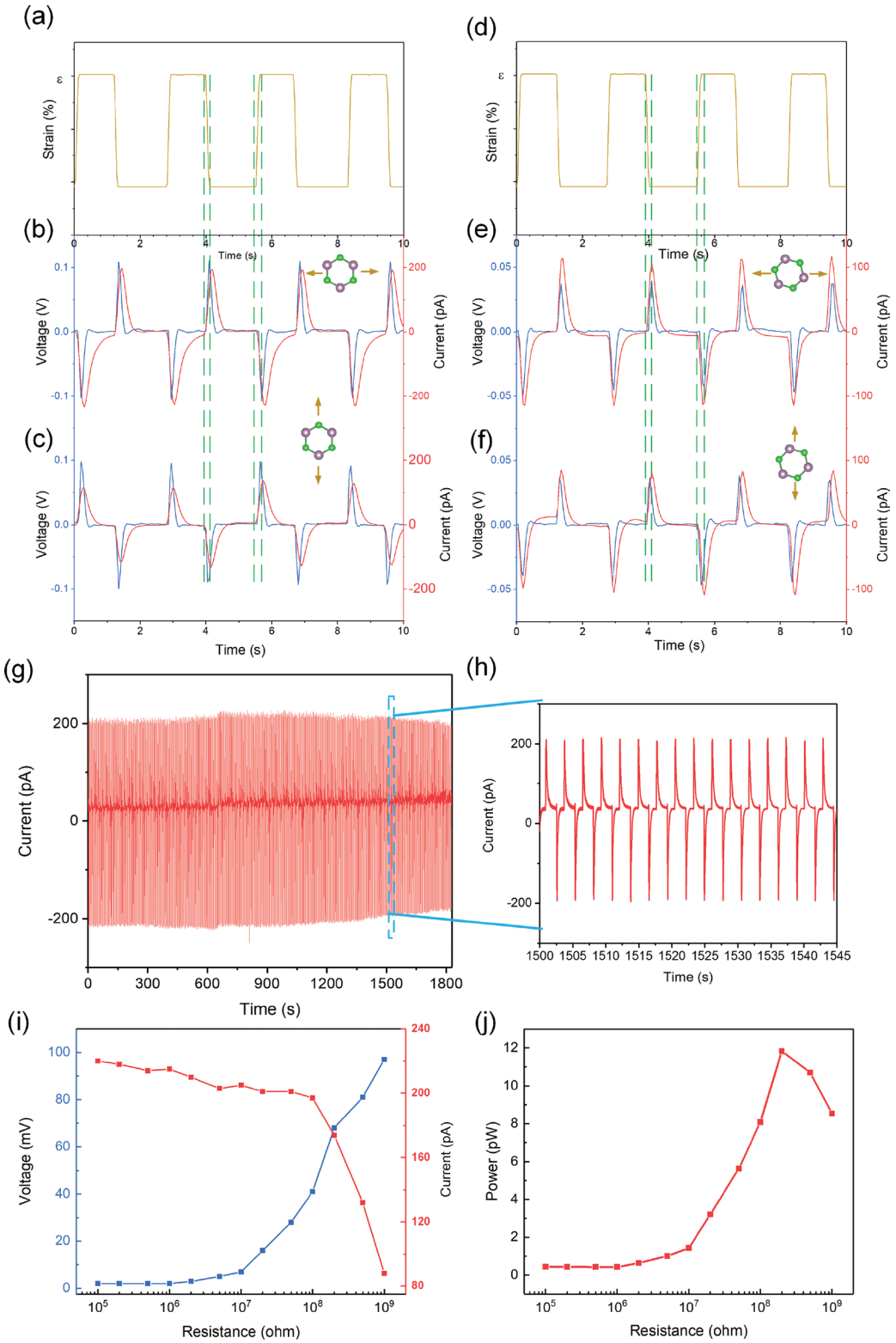

Figure 3. The piezoelectricity of a 3R-MoS_2 flake under uniaxial strains. a,d) Applied strain as a function of time (four cycles). b,c) The open-circuit voltage and short-circuit current response versus applied strains along *x* and *y* axis, respectively, for the aligned 3R-MoS_2 device. e,f) The open-circuit voltage and short-circuit current response versus applied strains along *x* and *y* axis, respectively, for the nonaligned 3R-MoS_2 device. g,h) Mechanical durability and stability test of an aligned MoS_2 flake under a strain of 0.47%: the output current as a function of time (left) and the extracted output current from 1500 s to 1545 s (right). i) The piezoelectric peak output voltage and current and j) the instantaneous power of the aligned 3R-MoS_2 flake as a function of the external loading resistance.

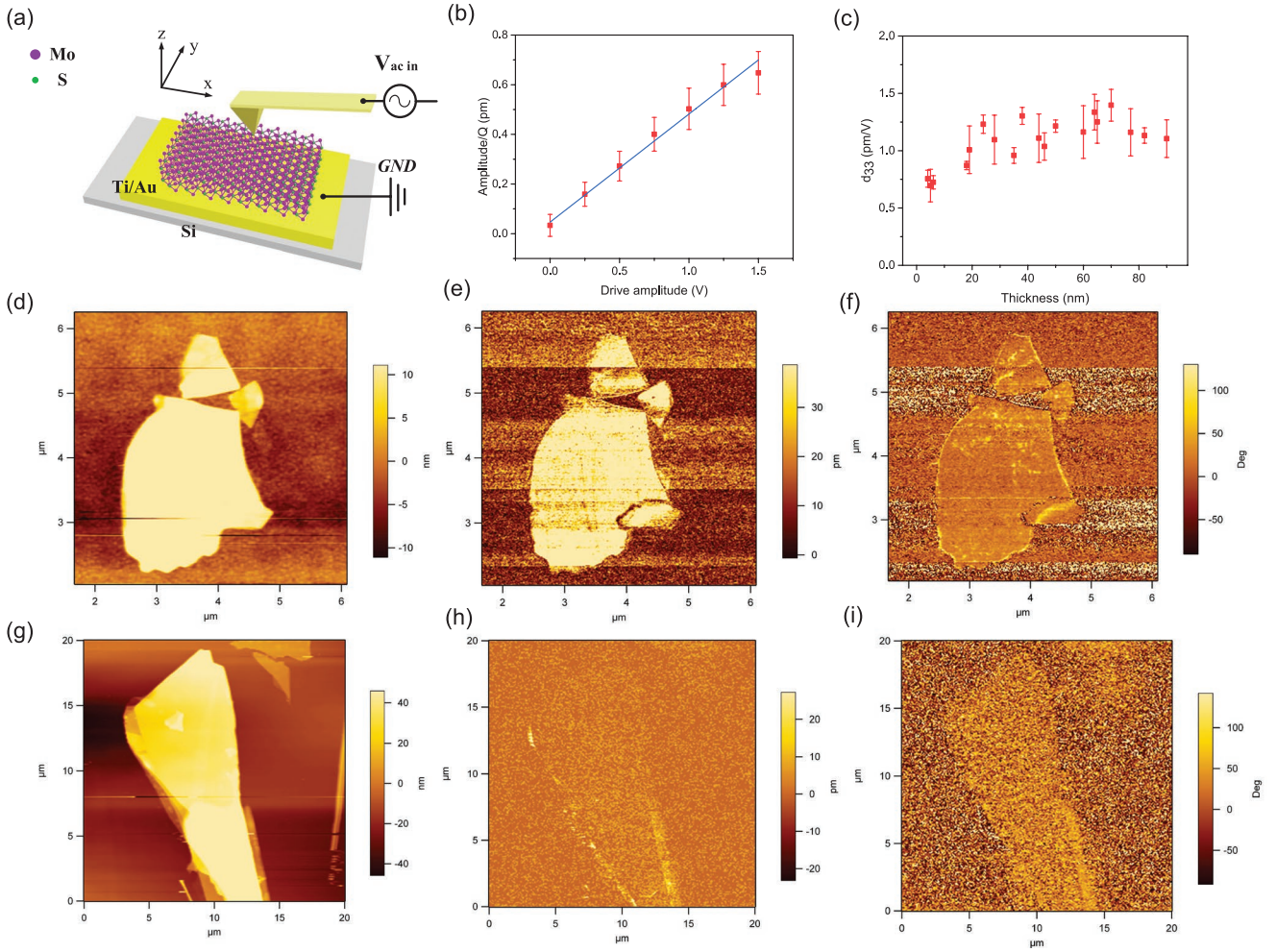

Figure 4. Out-of-plane piezo response study. a) Schematic of the experimental set-up of PFM study for the measurement of the out of plane piezoelectric coefficient d_{33}. b) The piezoresponse amplitude in the out of plane excitation (d_{33}) for the 18 nm 3R-MoS_2 flake as a function of the applied AC voltage. c) The d_{33} piezoelectric coefficients as a function of 3R MoS_2 flake thickness. d) The AFM topography image of a 18 nm 3R-MoS_2 flake. e,f) The PFM scan images of the out-of-plane piezoresponse-amplitude and phase, respectively, of the 18 nm 3R-MoS_2 flake in (d) at a bias voltage of 0.75 V. g) The AFM topography image of a 56 nm 2H-MoS_2 flake. h,i) The PFM scan images of the out-of-plane piezoresponse-amplitude and phase, respectively, of the g) 2H-MoS_2 flake at a bias voltage of 0.75 V.

amplitude and effective piezoelectric coefficient d_{eff} is given by the equation:

$$\text{Amplitude} = V_{\text{f}} \times \sigma = Q \times d_{\text{eff}} V_{\text{ac}} \tag{1}$$

where V_{f} is the vertical deflection signal, σ is the calibration constant of InvOLS, Q is the quality factor and V_{ac} is the applied AC bias voltage. The Q quality factor was obtained during AFM tuning. The AFM tip is in weak indentation with the flakes, therefore, the d_{33} and d_{eff} follow the relationship of: $d_{33} = 2 \times d_{\text{eff}}$.[46,47]

Measurement of the out-of-plane piezoresponse of an 18 nm 3R-MoS_2 flake is displayed in Figure 4b–e. Out-of-plane PFM piezoresponse phase and amplitude images showed a sharp contrast between the 3R-MoS_2 flakes and Ti/Au surface. A linear piezoresponse amplitude as a function of the AC bias voltage can be seen in Figure 4b, from which d_{eff} is estimated around 0.44 ± 0.02 pm V^{-1}, or d_{33} was around 0.88 ± 0.04 pm V^{-1}.

Furthermore, the d_{33} values as a function of the flake thickness are plotted in Figure 4c. It can be seen that the d_{33} value seemed to increase with the flake thickness and saturate around 1.0 pm V^{-1} for 3R-MoS_2 flakes thicker than 20 nm. It should be pointed out that these results are three to five times larger than the theoretical value of 0.27 pm V^{-1} predicted by Konabe and Yamamoto.[13] For comparison, 2H-MoS_2 flakes were also mechanically exfoliated and transferred on a Ti/Au surface for DART-PFM measurement and, in sharp contrast, they did not show a detectable out-of-plane piezoelectric response. As an example, a 56 nm 2H-MoS_2 flake (Figure 4g) could not produce an out-of-plane piezoresponse-amplitude and phase images under the same biased voltage of 0.75 V, as shown in Figure 4h,i.

To assess d_{13}, the ends of a 37 nm 3R-MoS_2 flake were buried with two metal electrodes and supplied with a voltage sweeping, see Figure 5a,c. The SHG intensity curve shows that the electrode edges were not perpendicular to the armchair or zigzag

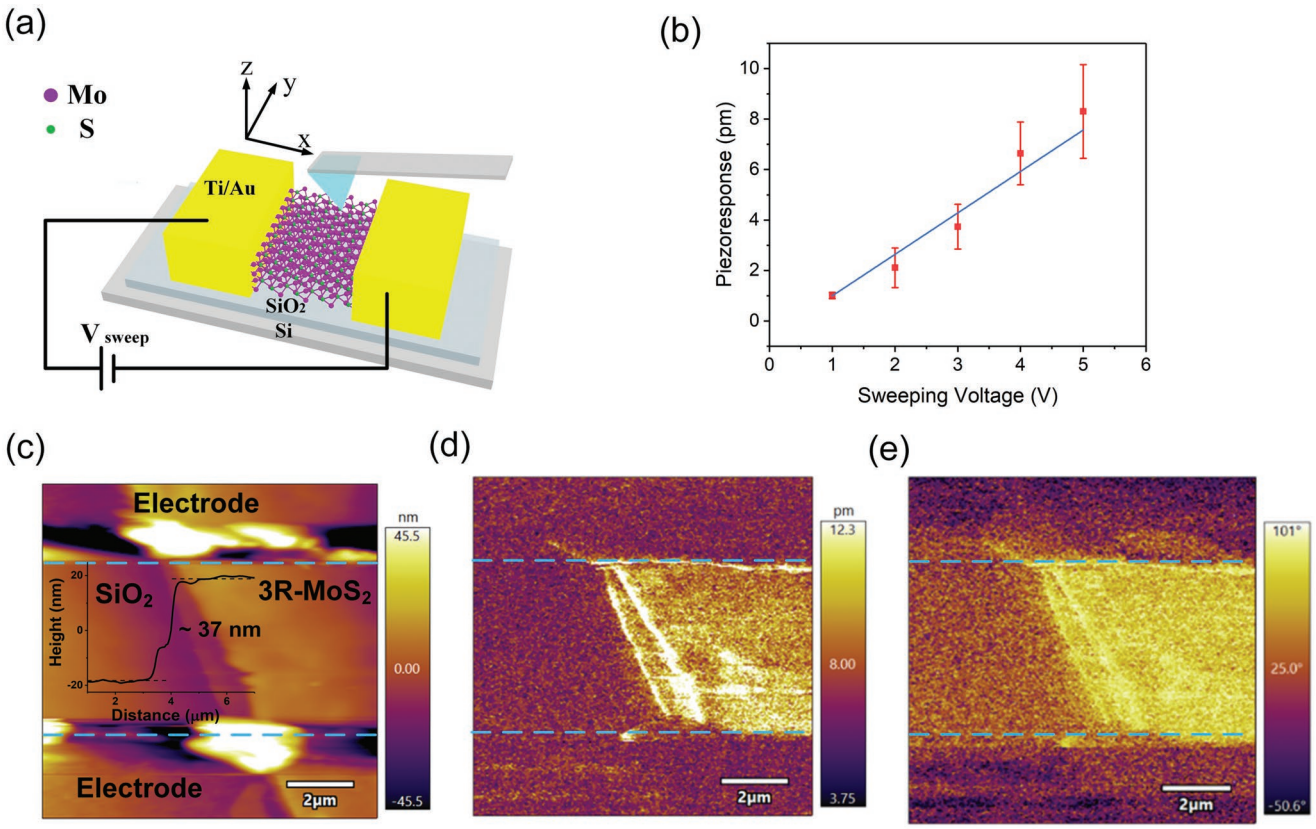

Figure 5. In-plane piezo response study. a) Schematic of the experimental set-up of PFM study for the measurement of the in plane piezoelectric coefficient d_{13}. b) The piezoresponse amplitude in the in-plane excitation d_{13} for the 37 nm 3R-MoS_2 flake as a function of the lateral excited bias voltage. c) The AFM topography image of a 37 nm 3R-MoS_2 flake with two electrodes. d,e) The PFM scan images of the piezoresponse amplitude and phase, respectively, under a lateral excited bias voltage of 3.0 V.

directions for the 37 nm 3R-MoS_2 flake, as shown in Figure S5 (Supporting Information). The lateral electric field induced the in-plane strain could lead to out-of-plane detectable mechanical deformation, which could be probed by the nonconductive tip. Figure 5c,d shows clear piezoresponse amplitude and phase images when a voltage of 3 V was applied to the two electrodes. From the linear dependence of the lateral excited piezo amplitude as a function of the applied voltage (Figure 5b), the piezoelectric coefficient d_{13} can be estimated around 1.64 ± 0.16 pm V^{-1}. These experimental results suggest that 3R-MoS_2 flakes are of the in-plane and out-of-plane piezoelectricity, irrespective of the thickness. By contrast, no piezo response was observed from the dummy sample with only electrodes and a 99 nm 2H-MoS_2 flake when they were subject to the same lateral electric field as that used for the 37 nm 3R-MoS_2 flake (Figures S6 and S7, Supporting Information), owing to its centrosymmetry structure.

To our best knowledge, no systematic experimental study has been reported on 3R-MoS_2 flakes until now. Recent theoretical study of piezoelectricity in 3R-MoS_2 using the molecular dynamics computational package LAMMPS[28] has emphasized that 3R-MoS_2 with five layers would show the highest direct piezoelectric constant (e_{11} = 0.457 C m^{-2}), approximately 13% than that of monolayer MoS_2 (e_{11} = 0.406 C m^{-2}). The piezoelectric constant would then slowly decrease with increasing the layer number. Interestingly, in our study, different 3R-MoS_2 flakes with the thickness from 4 to 90 nm, or ≈6 to ≈128 layers of MoS_2 monolayer (≈ 0.7 nm), [11] were employed for the d_{33} assessment and the out of plane piezoelectric coefficient was found within a range from 0.7 ± 0.2 to 1.5 ± 0.2 pm V^{-1}. When the thickness of 3R-MoS_2 flakes was decreased to ≈4 nm, the piezoelectric coefficient d_{33} was measured smaller than that of thicker 3R-MoS_2 flakes, which might reflect the influences of the substrate on d_{33} for the thinner flakes.[32] Note that, in the theoretical study,[28] the direct piezoelectric constant (e_{11}) was calculated instead of reverse piezoelectric coefficients in the lateral and out of plane excitation. In addition, several assumptions and approximations were introduced, while the treatment of complicated mixture of surface effects, electronic interactions, and atomistic structure details may not be taken into a full consideration due to capability restriction.[27] Thus, a detailed comparison between the reported theoretical results and our experimental observations still requires precaution at this stage.

3. Conclusion

In this study, the strong piezoelectricity of 3R-MoS_2 flakes is clearly observed for the first time. The symmetry broken in 3R-MoS_2 flakes is evidenced using second-harmonic

generation microscopy. Piezoelectric polarization charges are detected in 3R-MoS_2 flakes once they are strained in the armchair direction. Both amplitude and phase piezoresponses of 3R-MoS_2 flakes to the applied electric field are very strong. The piezoelectric coefficient d_{33} is estimated to be ≈0.9 pm V^{-1} for the 18 nm 3R-MoS_2 flakes. In addition, the d_{13} is estimated to be ≈1.6 pm V^{-1} for the 37 nm 3R-MoS_2 flakes. These coefficients are not apparently dependent on the thickness of the flakes.

4. Experimental Section

Samples Fabrication for Direct Piezoelectricity and PFM Measurements: The 3R-MoS_2 flakes were transferred to soft and hard substrates to characterize mechanical stress-induced piezoelectric signals and piezoelectric coefficients d_{33} and d_{13} (see Figure S8, Supporting Information).

A 125 µm polyimide substrate was first cleaned with acetone, isopropyl, and deionized water. The 3R-MoS_2 flakes from the grown single crystals described in ref. 20 were mechanical exfoliated onto a polyimide substrate. Then, an Au thin film (150 nm) was deposited by an electron beam evaporator (Edwards Auto 360), followed by an etch-down process to define a pair of electrodes on the two terminals of the 3R-MoS_2 flakes.

A 280 nm silicon oxide coated silicon wafer (500 µm) was first cleaned with acetone, isopropyl, and deionized water. The 3R-MoS_2 flakes from the CVD grown single crystals were mechanically exfoliated onto the SiO_2/Si substrate. Then, a Ti/Au thin film (20/150 nm) was deposited by an electron beam evaporator, followed by a lift-off process to define a pair of electrodes on the two terminals of the 3R-MoS_2 flakes. Before the PFM measurements, the devices were cleaned by nitrogen gas blow for 2–3 min.

For the samples dedicated for the out-of-plane piezoelectric coefficient, a SiO_2/Si substrate was first cleaned as described above and mechanically exfoliated 3R-MoS_2 flakes onto the substrate. A layer of PMMA was spin-coated on the samples at 3000 rpm for 45 s, and then prebaked at 105 °C for 5 min. The KOH solution was adopted as the etchant to remove the SiO_2 layer and release the PMMA/3R-MoS_2 flakes from the Si substrate. The flakes were then transferred on a Ti/Au thin film (20/150 nm) coated silicon wafer. Then, the PMMA was dissolved in acetone solution. Before the measurement, the sample was annealed in argon gas at 180 °C for 1.5 h.

For comparison purpose, several 2H-MoS_2 counterpart samples were also prepared under the same processing conditions as 3R-MoS_2 samples described above.

PFM Investigations—Calibration of PFM: The Asylum Research Periodically Poled Lithium Niobate (AR-PPLN) was employed to calibrate our Asylum Research PFM. The reference sample has stripe domains that were permanently polarized for easy calibration and optimization of PFM parameters. It consisted of a 3 mm × 3 mm × 0.5 mm $LiNbO_3$ transparent die. Alternating patterns of oppositely poled stripe domains were in parallel to the one axis of the die. The pitch of the domains was 10 µm. (see Figures S9 and S10, Supporting Information).

PFM Investigations—Measurement of the Out-of-Plane Piezo Coefficient (d_{33}): The out-of-plane piezoelectric coefficient measurements were performed using the same Asylum AFM with a dual AC resonance tracking PFM mode (DART-PFM). A Pt/Ir coated conductive tip with a force constant of 2.8 N m^{-1} was used to apply an electric field through the 3R-MoS_2 flakes by applying an AC voltage sweeping from 0 to 1.5 V at a step of 0.25 V between the tip and the back electrode. The deflection of the conductive tip caused by the expansion and contraction of the flakes reveals the different amplitude and phase of the piezo generated vertical displacement. Concurrently, the distribution of vertical displacement was recorded in the amplitude and the phase images as a function of the applied voltage. The average of piezoresponse amplitude was estimated using AFM Analysis software. The nanoscale images of amplitude were analyzed and used to calculate the out-of-plane piezo coefficient (see Figure S11, Supporting Information).

PFM Investigations—Measurement of the Lateral Piezo Coefficient (d_{13}): The lateral piezoelectric coefficient measurements were performed with a single frequency PFM mode using a nonconductive tip with a very low force constant of 10 to 130 N m^{-1}. Here, the non-conductive tip was used to measure only the deformation of the 3R-MoS_2 flakes by applying a voltage sweeping (AC signal) from 1 to 5 V through the electrodes covered the ends of the 3R-MoS_2 flakes on SiO_2 substrates. Then, the surface of the samples was scanned with the tip. The amplitude and the phase images were analyzed with the same technique described above to calculate d_{33} (see Figure S12, Supporting Information).

Supporting Information

Supporting Information is available from the Wiley Online Library or from the author.

Acknowledgements

The authors are grateful for the financial supports: of the Singaporean grants from: MOE Tier 2 grant (MOE 2017-T2-2-136), A*STAR AME IRG Grant SERC A1983c0027, Singapore and French National Research Agency under Project ANR-13-BS03-0010 and the "Investments for the future" Programme IdEx Bordeaux, under Grant ANR-10-IDEX-03-02.

Conflict of Interest

The authors declare no conflict of interest.

Author Contributions

H.H. and W.C. contributed equally to this work. H.H., W.C., and Q.Z. conceived the study and wrote the manuscript and all authors revised the manuscript. H.H., with the help of W.C., fabricated samples and performed the piezoresponse force microscopy (PFM) experiments to characterize the piezoelectric coefficients d_{13} and d_{33}. W.C. and K.Z. fabricated samples and performed the direct piezoelectric measurement with the help of R.X., P.Y., C.Z., and L.Z. synthesized the 3R-MoS_2 materials, and provided the atomic resolution TEM imaging of the materials and structural analyses. S.L. and Q.X. performed SHG to determine the crystal orientation of the 3R-MoS_2 flakes.

Data Availability Statement

The data that support the findings of this study are available in the supplementary material of this article.

Keywords

piezoelectric coefficients, piezoelectric devices, piezoelectricity of 3R-MoS_2 flake, piezoresponse force microscopy (PFM), TMDs materials electrical properties

Received: October 16, 2021
Revised: January 21, 2022
Published online: February 16, 2022

[1] C. Zuo, C. He, W. Cheng, Z. Wang, presented at 2019 IEEE International Ultrasonics Symposium (IUS), Glasgow, Scotland, UK October **2019**.
[2] R. Lu, T. Manzaneque, Y. Yang, L. Gao, A. Gao, S. Gong, *IEEE Trans. Microwave Theory Tech.* **2019**, *67*, 1516.
[3] N. T. Otterstrom, R. O. Behunin, E. A. Kittlaus, Z. Wang, P. T. Rakich, *Science* **2018**, *360*, 1113.
[4] K. C. Balram, M. I. Davanco, J. D. Song, K. Srinivasan, *Nat. Photonics* **2016**, *10*, 346.
[5] S. A. Tadesse, M. Li, *Nat. Commun.* **2014**, *5*, 5402.
[6] M. Kaisti, T. Panula, J. Leppanen, R. Punkkinen, M. Jafari Tadi, T. Vasankari, S. Jaakkola, T. Kiviniemi, J. Airaksinen, P. Kostiainen, U. Meriheina, T. Koivisto, M. Pankaala, *npj Digital Med.* **2019**, *2*, 39.
[7] A. Mujahid, A. Afzal, F. L. Dickert, *Sensors* **2019**, *19*, 4395.
[8] W. Pang, H. Zhao, E. S. Kim, H. Zhang, H. Yu, X. Hu, *Lab Chip* **2012**, *12*, 29.
[9] K. Lange, B. E. Rapp, M. Rapp, *Anal. Bioanal. Chem.* **2008**, *391*, 1509.
[10] C.-B. Eom, S. Trolier-McKinstry, *MRS Bull.* **2012**, *37*, 1007.
[11] K. Liu, Q. Yan, M. Chen, W. Fan, Y. Sun, J. Suh, D. Fu, S. Lee, J. Zhou, S. Tongay, J. Ji, J. B. Neaton, J. Wu, *Nano Lett.* **2014**, *14*, 5097.
[12] A. Castellanos-Gomez, M. Poot, G. A. Steele, H. S. van der Zant, N. Agrait, G. Rubio-Bollinger, *Adv. Mater.* **2012**, *24*, 772.
[13] S. Konabe, T. Yamamoto, *Jpn. J. Appl. Phys.* **2017**, *56*, 098002.
[14] P. Sahatiya, C. Madhava, A. Shinde, S. Badhulika, *IEEE Trans. Nanotechnol.* **2018**, *17*, 338.
[15] S. K. Kim, R. Bhatia, T.-H. Kim, D. Seol, J. H. Kim, H. Kim, W. Seung, Y. Kim, Y. H. Lee, S.-W. Kim, *Nano Energy* **2016**, *22*, 483.
[16] S. Sahoo, A. P. S. Gaur, M. Ahmadi, M. J. F. Guinel, R. S. Katiyar, *J. Phys. Chem. C* **2013**, *117*, 9042.
[17] R. Yan, J. R. Simpson, S. Bertolazzi, J. Brivio, M. Watson, X. Wu, A. Kis, T. Luo, A. R. Hight Walker, H. G. Xing, *ACS Nano* **2014**, *8*, 986.
[18] J. J. Bae, H. Y. Jeong, G. H. Han, J. Kim, H. Kim, M. S. Kim, B. H. Moon, S. C. Lim, Y. H. Lee, *Nanoscale* **2017**, *9*, 2541.
[19] I. Jo, M. T. Pettes, E. Ou, W. Wu, L. Shi, *Appl. Phys. Lett.* **2014**, 104, 201902.
[20] R. W. Powell, C. Y. Ho, P. E. Liley, United States National Bureau of Standards, United States Department of Commerce, *Thermal Conductivity of Selected Materials*, U.S. Department of Commerce, National Bureau of Standards; for sale by the Superintendent of Documents, U.S. Govt. Print. Off., Washington **1966**.
[21] J. Shi, P. Yu, F. Liu, P. He, R. Wang, L. Qin, J. Zhou, X. Li, J. Zhou, X. Sui, S. Zhang, Y. Zhang, Q. Zhang, T. C. Sum, X. Qiu, Z. Liu, X. Liu, *Adv. Mater.* **2017**, *29*, 1701486.
[22] T. Jiang, H. Liu, D. Huang, S. Zhang, Y. Li, X. Gong, Y.-R. Shen, *Nat. Nanotechnol.* **2014**, *9*, 825.
[23] M. N. Blonsky, H. L. L. Zhuang, A. K. Singh, R. G. Hennig, *ACS Nano* **2015**, *9*, 9885.
[24] W. Wu, L. Wang, Y. Li, F. Zhang, L. Lin, S. Niu, D. Chenet, X. Zhang, Y. Hao, T. F. Heinz, J. Hone, Z. L. Wang, *Nature* **2014**, *514*, 470.
[25] J.-H. Lee, J. Y. Park, E. B. Cho, T. Y. Kim, S. A. Han, T.-H. Kim, Y. Liu, S. K. Kim, C. J. Roh, H.-J. Yoon, H. Ryu, W. Seung, J. S. Lee, J. Lee, S.-W. Kim, *Adv. Mater.* **2017**, *29*, 1606667.
[26] L. Samad, S. M. Bladow, Q. Ding, J. Zhuo, R. M. Jacobberger, M. S. Arnold, S. Jin, *ACS Nano* **2016**, *10*, 7039.
[27] D. Zhu, H. Shu, F. Jiang, D. Lv, V. Asokan, O. Omar, J. Yuan, Z. Zhang, C. Jin, *npj 2D Mater. Appl.* **2017**, 1, 8.
[28] D. Tan, M. Willatzen, Z. L. Wang, *Nano Energy* **2019**, *56*, 512.
[29] X. Zhang, J. Grajal, J. L. Vazquez-Roy, U. Radhakrishna, X. Wang, W. Chern, L. Zhou, Y. Lin, P. C. Shen, X. Ji, X. Ling, A. Zubair, Y. Zhang, H. Wang, M. Dubey, J. Kong, M. Dresselhaus, T. Palacios, *Nature* **2019**, *566*, 368.
[30] M. D. Nguyen, E. P. Houwman, G. Rijnders, *Sci. Rep.* **2017**, *7*, 12915.
[31] Y.-R. Jeng, P.-C. Tsai, T.-H. Fang, *Nanotechnology* **2004**, *15*, 1737.
[32] X.-W. Fu, Z.-M. Liao, R. Liu, J. Xu, D. Yu, *ACS Nano* **2013**, *7*, 8891.
[33] F. Casset, A. Devos, S. Sadtler, A. L. Louarn, P. Emery, G. L. Rhun, P. Ancey, S. Fanget, E. Defaÿ, presented at 2012 IEEE Int. Ultrasonics Symp., Dresden, Germany October **2012**.
[34] N. Kumar, S. Najmaei, Q. Cui, F. Ceballos, P. M. Ajayan, J. Lou, H. Zhao, *Phys. Rev. B* **2013**, 87, 161403.
[35] Y. Li, Y. Rao, K. F. Mak, Y. You, S. Wang, C. R. Dean, T. F. Heinz, *Nano Lett.* **2013**, *13*, 3329.
[36] L. Mennel, M. Paur, T. Mueller, *APL Photonics* **2019**, 4, 03440.
[37] L. M. Malard, T. V. Alencar, A. P. M. Barboza, K. F. Mak, A. M. de Paula, *Phys. Rev. B* **2013**, 87, 201401(R).
[38] W. Cai, J. Wang, Y. He, S. Liu, Q. Xiong, Z. Liu, Q. Zhang, *Nanomicro Lett.* **2021**, *13*, 74.
[39] F. Xue, J. Zhang, W. Hu, W. T. Hsu, A. Han, S. F. Leung, J. K. Huang, Y. Wan, S. Liu, J. Zhang, J. H. He, W. H. Chang, Z. L. Wang, X. Zhang, L. J. Li, *ACS Nano* **2018**, *12*, 4976.
[40] Y. Zhou, D. Wu, Y. Zhu, Y. Cho, Q. He, X. Yang, K. Herrera, Z. Chu, Y. Han, M. C. Downer, H. Peng, K. Lai, *Nano Lett.* **2017**, *17*, 5508.
[41] E. Nasr Esfahani, T. Li, B. Huang, X. Xu, J. Li, *Nano Energy* **2018**, *52*, 117.
[42] C. J. Brennan, R. Ghosh, K. Koul, S. K. Banerjee, N. Lu, E. T. Yu, *Nano Lett.* **2017**, *17*, 5464.
[43] A. Gomez, M. Gich, A. Carretero-Genevrier, T. Puig, X. Obradors, *Nat. Commun.* **2017**, *8*, 1113.
[44] ANSI/IEEE Std 176-1987 1988, https://doi.org/10.1109/IEEESTD.1988.796380_1. **1988**.
[45] V. Lindroos, M. Tilli, A. Lehto, T. Motooka, *Handbook of Silicon Based MEMS Materials and Technologies*, Elsevier, Amsterdam **2010**.
[46] X. Wang, X. He, H. Zhu, L. Sun, W. Fu, X. Wang, L. C. Hoong, H. Wang, Q. Zeng, W. Zhao, J. Wei, Z. Jin, Z. Shen, J. Liu, T. Zhang, Z. Liu, *Sci. Adv.* **2016**, *2*, e1600209.
[47] S. Jesse, A. P. Baddorf, S. V. Kalinin, *Nanotechnology* **2006**, *17*, 1615.